

# Non-invasive in silico determination of ventricular wall pre-straining and characteristic cavity pressures

Sebastian Skatulla<sup>1</sup>, Carlo Sansour<sup>2</sup>, Mary Familusi<sup>1,3</sup>, Jagir Hussan<sup>4</sup>, and Ntobeko Ntusi<sup>5,6,7,8</sup>

<sup>1</sup>Computational Continuum Mechanics Research Group, Department of Civil Engineering, University of Cape Town, South Africa

<sup>2</sup>Department of Mathematics, Bethlehem University, Bethlehem, Palestine

<sup>3</sup>South African DST-NRF Centre of Excellence in Epidemiological Modelling and Analysis, Stellenbosch University, South Africa

<sup>4</sup>Auckland Bioengineering Institute, University of Auckland, New Zealand

<sup>5</sup>Division of Cardiology, Department of Medicine, University of Cape Town, Cape Town, South Africa

<sup>6</sup>Cape Heart Institute, Faculty of Health Sciences, University of Cape Town, South Africa

<sup>7</sup>Cape Universities Body Imaging Centre, Faculty of Health Sciences, University of Cape Town, South Africa

<sup>8</sup>South African Medical Research Council Extramural Unit on Intersection of Noncommunicable Diseases and Infectious Diseases

August 3, 2023

## Abstract

The clinical application of patient-specific modelling of the heart can provide valuable insights in supplementing and advancing methods of diagnosis as well as helping to devise the best possible therapeutic approach for each individual pathological heart condition. The potential of computational cardiac mechanics, however, has not yet been fully leveraged due to the heart's complex physiology and limitations in the non-invasive in vivo characterisation of heart properties necessary required for accurate patient-specific modelling such as the heart anatomy in an unloaded

state, ventricular pressure, the elastic constitutive parameters and the myocardial muscle fibre orientation distribution. From a solid mechanics point of view without prior knowledge of the unloaded heart configuration and the cavity pressure-volume evolution, in particular, the constitutive parameters cannot be accurately estimated to describe the highly non-linear elastic material behaviour of myocardial tissue. Here, knowledge of the volume-normalized end-diastolic pressure relation for larger mammals is exploited in combination with a novel iterative inverse parameter optimisation framework to determine end-systolic and end diastolic pressures, ventricular wall pre-straining and pre-stressing due the residual end-systolic cavity pressure as well as myocardial tissue stiffness parameters for biventricular heart models.

## 1 Introduction

Realistic modelling of the whole beating heart is the "holy grail" of computational cardiac mechanics which has been achieved only recently by the international "Living Heart Project" research initiative Baillargeon et al. [2014]. The objective of patient-specific modelling of the heart, however, is still out of reach, because further intense research efforts are necessary to determine the biomechanical properties of healthy and diseased heart muscle tissue in-vivo, meaning non-invasive. The effective implementation and evaluation of the clinical use of patient-specific modelling supplementing personalized therapy is mostly unknown and under debate Gray and Pathmanathan [2018]. In patient-specific heart modelling, it is crucial to be able to calibrate the various model parameters to clinically observed data, because models can only be relied on and be used for prediction if an observed physiological state can be represented.

Patient-specific biomechanical modelling of the heart has to account for the presence of a physiological pressure load as a result of the pre-stressed state of the imaged tissue. Two main sources of pre-stressing need to be considered: Firstly, cardiac tissue exhibits growth- and remodelling-related residual stresses even if completely unloaded ex vivo Omens et al. [2003], Shi et al. [2019], Zhuan and Luo [2022] and secondly, anatomical heart models are usually based on in vivo imaging of the beating heart when exhibiting the lowest cavity pressures at end systole, see e.g. Nikou et al. [2016]. The latter implies that the heart tissue is still experiencing stress, strain and deformation due to the remaining pressure. Failure to account for this pre-stressed state in solid tissue mechanics models results in inaccurate metrics, which are then used for health evaluation, risk assessment, or surgical planning.

In solid mechanics, the load application and corresponding deformation, strain and stress response is analyzed as linked to the unloaded material configuration of the problem at hand. This requires knowledge of the unloaded configuration which is in cardiac mechanics typically unknown. However, with the knowledge of the residual cavity pressure, the unknown unloaded configuration of the heart can be found by solving an inverse problem based on its known pre-stressed configuration. This inverse problem can usually only be solved

computationally, in particular for biological tissue mechanics applications due to the highly nonlinear nature. Rajagopal et al. [2007] proposed an incremental and iterative method applying a finite difference approximation of the finite element (FE) residual vector formulated in the Lagrangian form to predict the undeformed shape of human breasts. Bols et al. [2013] proposed a backward displacement method making use of a fixed point algorithm to iteratively retrieve the in vivo stress in a mouse-specific abdominal aorta due to the blood pressure at the moment of imaging and to reinstate the zero-pressure blood vessel geometry. Using in-vivo pressure data and magnetic resonance imaging, Pourmodheji et al. [2021] applied a patient-specific inverse FE modelling framework to iteratively determine besides the elastic material parameters the pre-stretch of elastin and collagen fibres in the proximal pulmonary arteries in order to assess mechanical and structural alterations of these micro-constituents. In contrast, a direct approach requires the governing equations to be consistently related to the known deformed configuration. Accordingly, Govindjee and Mihalic [1996] and Gee et al. [2010] derived the corresponding weak form as integrals over the current body. Govindjee and Mihalic also elaborated on the difficulty concerning a conservative traction boundary condition when related to quantities defined in current configuration. Applying this approach to a biventricular heart model, it was shown that the inclusion of pre-stressing leads to significant strain contributions in the myocardium Peirlinck et al. [2018]. In the work of Hirschvogel et al. [2017] the imaging-based patient-specific ventricular model was pre-stressed to low end-diastolic pressure to account for the imaged, stressed configuration, using a modified updated Lagrangian FE formulation proposed by Gee et al. [2010] where on element level only the deformation gradient and the isoparametric Jacobian matrix was updated.

The modelling of the deformation response of biological tissue to the applied loading additionally requires the determination of the parameters of the non-linear elastic material relations. Initially, patient-specific mechanical properties of blood arteries were estimated by analytical equations such as the Young-Laplace Law. However, the underlying assumptions of material homogeneity and isotropy contradict the known complexity of myocardial and vascular tissue Moulton et al. [1995]. Klotz et al. [2006] uncovered from ex vivo and in vivo measurements of end diastolic pressure volume relations (EDPVR) and subsequent regression analysis that normalized EDPVR curves of the left ventricle (LV) had a consistent profile across humans and a variety of mammals, regardless of etiology. Using the least-squared error between the so-called "Klotz curve" and the modelled ventricular pressure-volume curve as an optimization objective increases the number of comparison points and facilitates the fitting of non-linear myocardial material models, e.g. Genet et al. [2014], Palit et al. [2018], Sack et al. [2018]. The use of the "Klotz curve" requires at least one measured pressure-volume pair which is usually the end diastolic pressure and volume. However, in cardiac mechanics specifically, the in vivo patient-specific LV pressure is often not known as well, because the only accurate method for LV pressure measurement is invasive catheterization which is therefore not readily available on an individual basis. Without prior knowledge of the so-called end-

diastolic pressure-volume relation, it is effectively not possible to calibrate the anisotropic highly non-linear elastic material relations for myocardial tissue.

To address the problem when direct pressure measurements are unavailable, this work proposes to combine a direct inverse method to determine the unloaded configurations of biventricular patient-specific heart models with the previously mentioned "Klotz curve" and the bounded Levenberg-Marquart parameter optimisation method. This allows for the simultaneous computation of the unknown end-diastolic ventricular pressures, pre-stressing and elastic material constants. In contrast to the related inverse unloaded configuration determination approaches by Govindjee and Mihalic [1996] and Gee et al. [2010], the variational principle in the known deformed configuration is derived from the conventional Lagrangian formulation.

The paper is organized as follows: In Sec. 2 the basics of a standard total Lagrangian approach are revised. Based on this, a non-standard total Lagrangian approach is introduced in Sec. 3 which allows for direct computation of the unloaded configuration based on a known loaded configuration. Finally, in Sec. 5 the proposed method is applied to three numerical examples modelling non-linear hyperelastic material.

## 2 Standard total Lagrangian approach

This section provides only in brief the basic principles of a total Lagrangian approach including necessary kinematical assumptions, variational principle and its governing equations. For further details the reader is referred to e.g. ?.

### 2.1 Kinematics

Let  $\mathbb{E}(3)$  be the Euclidian vector space and  $\mathcal{B} \subset \mathbb{E}(3)$ , where  $\mathcal{B}$  is a three-dimensional manifold defining a material body. A motion of  $\mathcal{B}$  is represented by a one parameter non-linear deformation mapping  $\varphi_t : \mathcal{B} \rightarrow \mathcal{B}_t$ , where  $t \in \mathbb{R}$  is the time and  $\mathcal{B}_t$  is the current configuration at time  $t$ . Accordingly, each material point  $\mathbf{X} \in \mathcal{B}$  is related to its placement  $\mathbf{x}$  in the spatial configuration  $\mathcal{B}_t$  by the mapping

$$\mathbf{x} = \varphi(\mathbf{X}, t) \tag{1}$$

In what follows and without loss of generality we identify the body  $\mathcal{B}$  with its undeformed reference configuration at a fixed time  $t_0$ . The deformation map possesses an invertible linear tangent map  $\mathbf{F} = \text{Grad} \varphi$  denoted by the deformation gradient, where the Jacobian  $J = \det \mathbf{F} > 0$ . The operator Grad represents the gradient with respect to the reference configuration

$$\text{Grad} := \frac{\partial}{\partial \mathbf{X}}. \tag{2}$$

The body  $\mathcal{B}$  is parameterized by the Cartesian coordinates  $X_i$ ,  $i = 1, 2, 3$ . Here, and in what follows, Latin indices take the values 1, 2 or 3. As a deformation

measure we make use of the right *Cauchy-Green* deformation tensor  $\mathbf{C}$  defined by

$$\mathbf{C} = \mathbf{F}^T \mathbf{F}. \quad (3)$$

In the following we want to confine ourselves to the quasi static case.

## 2.2 Variational principle

Let us consider a non-linear boundary value problem on domain  $\mathcal{B}$  with boundary  $\partial\mathcal{B}$ . Dirichlet boundary conditions are prescribed on  $\partial\mathcal{B}_D \subset \partial\mathcal{B}$  and Neumann boundary conditions are prescribed on  $\partial\mathcal{B}_N = \partial\mathcal{B} \setminus \partial\mathcal{B}_D$ . We define the external virtual work in the Lagrangian form as follows

$$\mathcal{W}_{ext} = \int_{\mathcal{B}} \mathbf{b} \cdot \delta \mathbf{u} \, dV + \int_{\partial\mathcal{B}_N} \mathbf{t}^{(\mathbf{n})} \cdot \delta \mathbf{u} \, dA \quad (4)$$

where  $\mathbf{b}$  denotes the body force,  $\mathbf{t}^{(\mathbf{n})}$  the external traction and  $\mathbf{n}$  the outward normal on  $\partial\mathcal{B}_N$ .

Furthermore, we assume now that the body under consideration  $\mathcal{B}$  is hyperelastic and possesses an elastic potential  $\Psi$  represented by the stored strain energy per unit mass  $\psi(\mathbf{C})$ . The variation of the internal potential with respect to  $\mathbf{C}$  in the Lagrangian form reads as follows

$$\delta\Psi = \int_{\mathcal{B}} \rho_0 \frac{\partial\psi}{\partial\mathbf{C}} : \delta\mathbf{C} \, dV. \quad (5)$$

In the static case and by considering only mechanical processes the *first law of thermodynamics* provides the following variational statement

$$\delta\Psi - \mathcal{W}_{ext} = 0. \quad (6)$$

Upon substitution of Eqs. (4) and (5) this variational statement can be written as

$$\int_{\mathcal{B}} \frac{1}{2} \mathbf{S} : \delta\mathbf{C} \, dV - \int_{\mathcal{B}} \mathbf{b} \cdot \delta \mathbf{u} \, dV - \int_{\partial\mathcal{B}_N} \mathbf{t} \cdot \delta \mathbf{u} \, dA = 0, \quad (7)$$

with the second *Piola-Kirchhoff* stress tensor  $\mathbf{S}$  given by

$$\mathbf{S} = 2\rho_0 \frac{\partial\psi}{\partial\mathbf{C}}. \quad (8)$$

The governing equations of the above variational formulation (Eq. 7) can be derived by applying *Gauss's divergence theorem* and, assuming the variation  $\delta \mathbf{u} = \mathbf{0}$  on  $\partial\mathcal{B}_D$  but otherwise arbitrary, we have

$$\text{Div}(\mathbf{FS}) + \mathbf{b} = \mathbf{0} \quad \text{on } \mathcal{B}, \quad (9)$$

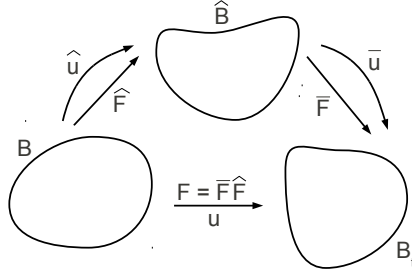


Figure 1: Configuration spaces.

and the corresponding Neumann boundary condition is given by

$$\mathbf{F}\mathbf{S}\mathbf{n} = \mathbf{t}^{(n)} \quad \text{on } \partial\mathcal{B}_N. \quad (10)$$

where  $\text{Div}$  denotes the divergence operator in the reference configuration. These field equations are supplemented by essential boundary conditions, the so-called Dirichlet boundary conditions

$$\mathbf{u} = \mathbf{g} \quad \text{on } \partial\mathcal{B}_D. \quad (11)$$

with  $\mathbf{g}$  being the displacement field prescribed on  $\partial\mathcal{B}_D$ .

### 3 Non-standard total Lagrangian approach

If the unloaded and stress-free configuration  $\mathcal{B}$  is not known but only a certain deformed configuration  $\hat{\mathcal{B}}$ , the standard total Lagrangian approach as introduced in the previous section cannot be directly used but needs to be modified. The reason for this is found in the fact that in the total Lagrangian approach the displacement field and its gradient as well as stress and strain quantities refer to the reference configuration which is unknown.

In order to proceed let us first introduce some deformation maps: As proposed by Gee et al. [2010] the unknown reference configuration  $\mathcal{B}$  is linked with the known deformed configuration  $\hat{\mathcal{B}}$  by  $\hat{\mathbf{F}}$  and any subsequent deformed configuration  $\mathcal{B}_t$  by  $\bar{\mathbf{F}}$ . Thus,

$$\mathbf{F} = \bar{\mathbf{F}}\hat{\mathbf{F}} = \frac{\partial \mathbf{x}}{\partial \hat{x}_i} \frac{\partial \hat{x}_i}{\partial \mathbf{X}} \quad (12)$$

relates  $\mathcal{B}$  with  $\mathcal{B}_t$  as illustrated in Fig. 1.

### 3.1 Inverse problem

First, the objective is to find

$$\hat{\mathbf{F}} = \frac{\partial \hat{\mathbf{x}}}{\partial \mathbf{X}} \quad (13)$$

with  $\hat{\mathbf{x}} \in \hat{\mathcal{B}}$  being known which we want to call "*inverse problem*". For this the standard variational principle needs to be reformulated such as to determine  $\mathbf{X} \in \mathcal{B}$  by employing the inverse of the tangent map (Eq. 13)

$$\hat{\mathbf{F}}^{-1} = \frac{\partial(\hat{\mathbf{x}} - \hat{\mathbf{u}})}{\partial \hat{\mathbf{x}}}, \quad (14)$$

where the displacement field  $\hat{\mathbf{u}}$  translates  $\mathcal{B}$  to the  $\hat{\mathcal{B}}$ .

Let us start with the standard variational formulation in its Lagrangian form (Eq. 7) evaluated when  $\mathcal{B}$  is deformed into  $\hat{\mathcal{B}}$  such that it holds  $\mathbf{F} = \hat{\mathbf{F}}$ :

$$\int_{\mathcal{B}} \hat{\mathbf{F}} \mathbf{S} : \delta \hat{\mathbf{F}} dV - \mathcal{W}_{ext} = 0 \quad (15)$$

where the second *Piola-Kirchhoff* stress tensor is now a function of  $\hat{\mathbf{C}} = \hat{\mathbf{F}}^T \hat{\mathbf{F}}$ , i.e.

$$\mathbf{S} = 2\rho_0 \frac{\partial \psi(\hat{\mathbf{C}})}{\partial \hat{\mathbf{C}}}. \quad (16)$$

From

$$\hat{\mathbf{F}} \hat{\mathbf{F}}^{-1} = \mathbf{1}$$

which is varied with respect to  $\hat{\mathbf{u}}$

$$\delta \hat{\mathbf{F}} \hat{\mathbf{F}}^{-1} + \hat{\mathbf{F}} \delta \hat{\mathbf{F}}^{-1} = \mathbf{0}$$

we obtain

$$\delta \hat{\mathbf{F}} = -\hat{\mathbf{F}} \delta \hat{\mathbf{F}}^{-1} \hat{\mathbf{F}}. \quad (17)$$

This is substituted together with  $dV = \hat{J}^{-1} d\hat{v}$  into the above standard variational formulation (Eq. 15) and we have

$$\int_{\hat{\mathcal{B}}} -\hat{J}^{-1} \hat{\mathbf{C}} \hat{\mathbf{S}} \hat{\mathbf{F}}^T : \delta \hat{\mathbf{F}}^{-1} d\hat{v} - \mathcal{W}_{ext} = 0, \quad (18)$$

which is with Eq. (14) and the Cauchy stress tensor given by  $\hat{\boldsymbol{\sigma}} = -\hat{J}^{-1} \hat{\mathbf{C}} \hat{\mathbf{S}} \hat{\mathbf{F}}^T$  analog to Gee et al. [2010], Govindjee and Mihalic [1996], Peirlinck et al. [2018]. Here, it is important to note that, as the integration needs to be performed over  $\hat{\mathcal{B}}$ , the approximation of geometry refers to  $\hat{\mathbf{x}} \in \hat{\mathcal{B}}$  and corresponding spatial derivatives  $\frac{\partial}{\partial \hat{\mathbf{x}}}(\bullet)$ .

In terms of loading, we need discriminate between conservative and non-conservative loading, i.e. whether it depends on deformation using the standard total Lagrangian approach (Eq. 7). For non-conservative loading, e.g. pressure loading  $p$ , using *Nanson's* formula  $\hat{\mathbf{n}} d\hat{a} = \hat{J}\hat{\mathbf{F}}^{-T}\mathbf{n} dA$  which establishes a relation between known deformed and corresponding unknown undeformed surface elements  $d\hat{\mathbf{a}}$  and  $d\mathbf{A}$ , respectively, the external virtual work is expressed in the unknown undeformed configuration as

$$\mathcal{W}_{ext} = \int_{\partial\mathcal{B}_N} p \hat{J}\hat{\mathbf{F}}^{-T}\mathbf{n} \cdot \delta\hat{\mathbf{u}} dA \quad (19)$$

whereas in the known deformed configuration as

$$\mathcal{W}_{ext} = \int_{\partial\hat{\mathcal{B}}_N} p \hat{\mathbf{n}} \cdot \delta\hat{\mathbf{u}} d\hat{a} \quad (20)$$

with  $\hat{\mathbf{n}}$  denoting the normal vector on  $\partial\hat{\mathcal{B}}$  which does not depend on the deformation. The latter is a crucial point to realize, as it is in contrast to standard total Lagrangian approach. When dealing with the inverse problem  $\hat{\mathcal{B}}$  is assumed fixed whereas  $\mathcal{B}_0$  needs to be incrementally approached due to the nonlinear nature of the problem. Consequently, when solving the the variational problem (Eq. 18) numerically, e.g. employing the Newton-Raphson method, the pressure does not appear in the variational statement's linearized form. Conversely, when applying a conservative loading, e.g. a traction force acting on the undeformed surface  $\partial\mathcal{B}_N$ , we have

$$\mathcal{W}_{ext} = \int_{\partial\mathcal{B}_N} \mathbf{t} \cdot \delta\hat{\mathbf{u}} dA \quad (21)$$

or with respect to the known deformed surface  $\partial\hat{\mathcal{B}}_N$

$$\int_{\partial\hat{\mathcal{B}}_N} \mathbf{t} \cdot \delta\hat{\mathbf{u}} \hat{J}^{-1} |\hat{\mathbf{F}}^T \hat{\mathbf{n}}| d\hat{a} \quad (22)$$

where the sizes of undeformed and deformed surface elements can be obtained from *Nanson's* formula  $|\mathbf{n}| dA = \hat{J}^{-1} |\hat{\mathbf{F}}^T \hat{\mathbf{n}}| d\hat{a}$ . Consequently, for inverse problem the linearization of the surface traction contribution (Eq. 22) does not vanish.

### 3.2 Forward problem

Once the map  $\hat{\mathbf{F}}$  linking unknown undeformed configuration  $\mathcal{B}_0$  and known deformed configuration  $\mathcal{B}$  has been determined as described in Sec. 3.1, any subsequent loading application which we want to term "*forward problem*" can be dealt with computing the total deformation gradient according to  $\mathbf{F} = \hat{\mathbf{F}}\hat{\mathbf{F}}$  where  $\hat{\mathbf{F}}$  is a function of the displacement increment  $\hat{\mathbf{u}}$  due to some additional loading and  $\hat{\mathbf{F}}$  remains constant. In practise, when employed to a numerical



method,  $\hat{\mathbf{F}}$  needs to be stored at all points of interest, e.g. numerical integration points.

Now, for forward problem the original variational formulation (Eq. 7) is reformulated with  $dV = \hat{J}^{-1}d\hat{v}$  as follows:

$$\int_{\hat{\mathcal{B}}} \hat{J}^{-1} \mathbf{F} \hat{\mathbf{S}} \hat{\mathbf{F}}^T : \delta \bar{\mathbf{F}} d\hat{v} - \mathcal{W}_{ext} = 0 \quad (23)$$

where the variation of  $\mathbf{F}$  expressed as

$$\delta \mathbf{F} = \delta \bar{\mathbf{F}} \hat{\mathbf{F}}. \quad (24)$$

For the latter it is important to realize that, as  $\hat{\mathbf{F}}$  is constant during the subsequent "forward" computation, the variation is only performed with respect  $\bar{\mathbf{u}} = \mathbf{x} - \hat{\mathbf{x}}$ , as  $\bar{\mathbf{F}} = \bar{\mathbf{F}}(\bar{\mathbf{u}})$  is linking  $\hat{\mathcal{B}}$  and  $\mathcal{B}_t$ .

With regards to deformation dependent loading we consider

$$\mathcal{W}_{ext} = \int_{\partial \hat{\mathcal{B}}_N} p \bar{J} \bar{\mathbf{F}}^{-T} \hat{\mathbf{n}} \cdot \delta \bar{\mathbf{u}} d\hat{a} \quad (25)$$

using *Nanson's* formula  $\bar{\mathbf{n}} d\bar{a} = \bar{J} \bar{\mathbf{F}}^{-T} \hat{\mathbf{n}} d\hat{a}$  which establishes the relation between unknown deformed and corresponding known deformed surface elements  $d\bar{\mathbf{a}}$  and  $d\hat{\mathbf{a}}$ , respectively. For deformation independent traction loading (Eq. (22)) still applies. Consequently, for the forward problem, as for the standard total Lagrangian approach, the pressure contribution (Eq. (25)) is to be linearized with respect to  $\bar{\mathbf{u}}$  whereas the linearization of the surface traction contribution does vanish, as  $\hat{\mathbf{F}}$  is now constant.

## 4 Inverse parameter optimisation method

As previously mentioned, the determination of elastic myocardial material parameters requires knowledge of ventricular filling pressure and corresponding deformation. The latter can include deformation metrics such as change of cavity volume, short-axis and long-axis cavity expansion, twisting about the long-axis or globally and regionally averaged myocardial strains, e.g. Genet et al. [2014], Palit et al. [2018], Sack et al. [2018].

Here, we aim at determining the elastic myocardial material parameters of biventricular (BV) models without prior knowledge of ventricular filling pressure data by exploiting the characteristic exponential nature of the "Klotz curve" fitted to three patient-specific left ventricular volume data, namely ESV and EDV from Cardiovascular Magnetic Resonance (CMR) imaging as well as the undeformed cavity volume,  $V_0$ , as obtained by inverse computation using the non-standard total Lagrangian approach presented in Sec. 3 implemented in a finite element method (FEM)-based code.

This is achieved by iterative parameter optimisation employing the Levenberg-Marquardt algorithm (LVM) Guyon and Le Riche [2000]. Further details regarding the specific LVM implementation can be found in Rama and Skatulla

[2019]. This iterative scheme is initialized by assuming a physiological EDP and elastic myocardial material parameters for the LV which serves to construct an initial volume-normalized "Klotz curve" Klotz et al. [2006]. Before elaborating on the details of the proposed iterative scheme, the important relations needed to set-up the "Klotz curve" are briefly summarized. Given a measured pair of LV cavity volume,  $V_m$ , and corresponding cavity pressure,  $P_m$ , the unloaded LV cavity volume can be estimated as

$$V_0 = V_m (0.6 - 0.006 P_m) \quad (26)$$

and at 30 mmHg as

$$V_{30} = V_0 + \frac{V_{m,n} - V_0}{(P_m/A_n)^{(1/B_n)}} \quad (27)$$

where the normalized measured volume is given by

$$V_{m,n} = \frac{V_m - V_0}{V_{30} - V_0} \quad (28)$$

and for humans the coefficients  $A_n = 27.8$  and  $B_n = 2.76$ . Then the EDPVR is formulated as

$$P_{LV} = \alpha V_{LV}^\beta \quad (29)$$

with

$$\alpha = \frac{30}{(V_{30})^{\text{Log}(P_m/30)/\text{Log}(V_m/V_{30})}} \quad (30)$$

and

$$\beta = \frac{\text{Log}(P_m/30)}{\text{Log}(V_m/V_{30})}. \quad (31)$$

Now, in the absence of LV pressure measurements, EDP is to be iteratively estimated taking  $P_m = \text{EDP}$  and  $V_m = \text{EDV}$ . For the initial setup of the "Klotz curve", a physiologically reasonable EDP value needs to be chosen. ESP and  $V_0$  can then be readily obtained via Eq. (29) knowing ESV from CMR and  $P_0 = 0$ . The LVM cost function considers the fitting error of  $V_0$  and EDV between "Klotz curve" and the FEM solution. As cavity pressure data are generally not available for the RV, it is therefore assumed that the "Klotz curve" (Eq. (29)) can provide an indication of the EDPVR of the RV as well. Due to this limitation, the LVM cost function only includes the error regarding EDV but not  $V_0$  for the RV. For each subsequent LVM iteration, updated elastic parameter and EDP values are obtained for LV and RV from the optimisation algorithm allowing for the update of the "Klotz curve" and subsequently ESP and  $V_0$  values as well. A noteworthy aspect of this approach is that the fitting target, which is the "Klotz curve", is continuously changing which is not the case in the standard application of LVM. The iterative parameter optimisation is terminated once the cost function error falls below a given threshold and the root-square error of the entire EDPVR of "Klotz curve" and FE simulation is smaller than 2.00 mmHg.

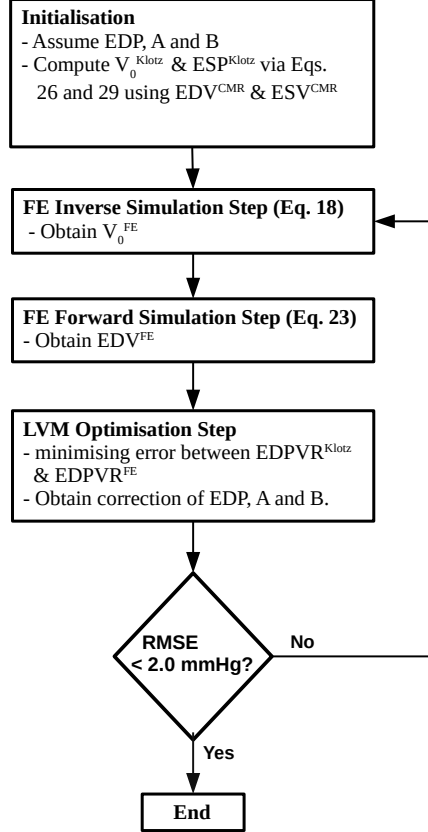


Figure 2: Inverse procedure combining "Klotz Curve", FE simulation and Levenberg-Marquardt (LVM) optimization schemes.

## 5 Numerical examples

The following examples presented in this section aim to demonstrate the potential of the proposed inverse parameter optimisation method outlined in Sec. 4. In this study, only the diastolic filling of the biventricular (BV) cavities will be examined.

We constructed patient-specific heart models of three healthy patients that were scanned using Cardiovascular Magnetic Resonance (CMR) imaging at the Groote Schuur Hospital, University of Cape Town, South Africa. University of Cape Town, Faculty of Health Sciences Human Research Ethics Committee approval (REF: 686/2018) and patients' consent were obtained to conduct research on unidentified human data. The left and right ventricular cavity volumes at end-systole and end-diastole, respectively, are presented in Tab. 1. The anatom-

Table 1: Ventricular cavity volumes measured by CMR.

	Left ventricle			Right ventricle		
	ESV	EDV	SV	ESV	EDV	SV
Case 1	90.00	168.00	78.00	61.00	96.00	78.00
Case 2	86.00	170.00	84.00	67.00	118.00	51.00
Case 3	82.00	157.00	75.00	78.00	160.00	82.00

ical models were meshed using 3326, 2765 and 3246 linear tetrahedral elements, for the cases 1, 2, and 3, respectively. ESP cavity filling pressure boundary conditions were applied to the endocardial surfaces of LV and RV according to Eq. (20) computing first the unloaded configuration as outlined in Sec. 3.1 and EDP cavity filling pressure boundary conditions according to Eq. (25) computing subsequently the end diastolic configuration as outlined in Sec. 3.2. In terms of the Dirichlet boundary conditions, the surface of the heart’s base is fixed to restrain vertical direction movement. To allow for torsional behaviour and wall thickening and thinning, a Dirichlet boundary condition is weakly imposed through application of an elastic line force of  $0.1kN$  acting in tangential direction around the epicardial base. The elastic line forces effectively prevent rigid body motion in short-axis directions as well.

The material behaviour of the BV heart muscle tissue is assumed to be nonlinear, anisotropic and nearly incompressible described by the following orthotropic strain energy function Usyk et al. [2000]

$$\psi = \frac{A}{2} \left( \exp^{BQ} - 1 \right) + A_{\text{comp}} \left( \det J \ln(\det J) - \det J + 1 \right), \quad (32)$$

where parameters  $A$  and  $B$  are stiffness factors and  $J = \det \mathbf{F}$  is the Jacobian quantifying volumetric deformation of cardiac tissue is linked to the constant  $A_{\text{comp}}$  controlling the compressibility of the myocardium. Additionally, the exponent  $Q$  is defined in terms of the Green strain tensor and the material directions defining structural tensors  $\mathbf{M}_f$ ,  $\mathbf{M}_s$  and  $\mathbf{M}_n$  as follows Rama et al. [2016]:

$$Q := a_1(\text{tr}(\mathbf{M}_f \mathbf{E}))^2 + a_2(\text{tr}(\mathbf{M}_s \mathbf{E}))^2 + a_3(\text{tr}(\mathbf{M}_n \mathbf{E}))^2 + a_4 \text{tr}(\mathbf{M}_f \mathbf{E}^2) + a_5 \text{tr}(\mathbf{M}_s \mathbf{E}^2) + a_6 \text{tr}(\mathbf{M}_n \mathbf{E}^2), \quad (33)$$

where  $a_i$ ,  $i = 1, \dots, 6$  are the anisotropy coefficients associated with the three preferred material directions, namely fiber axis,  $\mathbf{V}_f$ , sheet axis,  $\mathbf{V}_s$ , and sheet normal axis,  $\mathbf{V}_n$ . These vectors construct an orthonormal basis and allow for the formulation of the so-called structural tensors

$$\mathbf{M}_f = \mathbf{V}_f \otimes \mathbf{V}_f, \quad \mathbf{M}_s = \mathbf{V}_s \otimes \mathbf{V}_s, \quad \mathbf{M}_n = \mathbf{V}_n \otimes \mathbf{V}_n. \quad (34)$$

The values of the anisotropy material constants used are listed in Table 2.

The varying fibre directions throughout the LV and RV walls are computed adopting an algorithm developed by Wong and Kuhl Wenk et al. [2011] but

Table 2: Anisotropy coefficients used.

$A_{comp}$ (kPa)	$a_1$	$a_2$	$a_3$	$a_4$	$a_5$	$a_6$
100	6	7	3	12	3	3

using moving least square (MLS) based approximations as proposed by Skatulla and Sansour [2016] instead of the solving a Poisson problem. The resulting fibre direction distribution is shown for Case 2 in Fig. 3. The prescribed fibre direction angles at the endocardium and epicardium of both LV and RV are  $+72^\circ$  and  $-57^\circ$ , respectively Rama and Skatulla [2019].

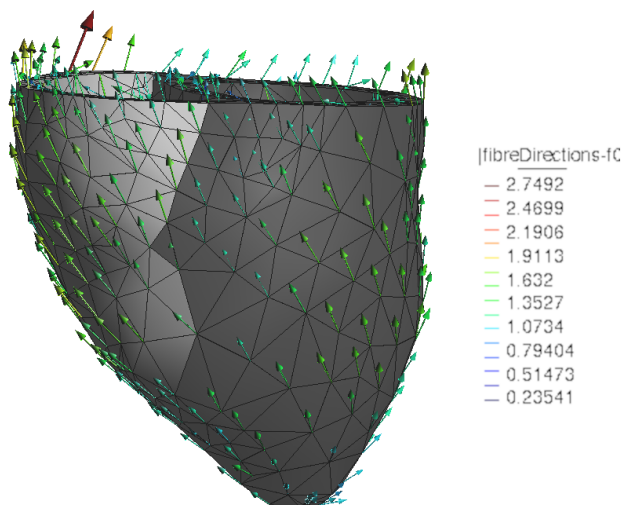


Figure 3: Myocardial fibre orientation of a bi-ventricular model.

## 5.1 Iterative parameter estimation

The iterative parameter estimation approach is used to obtain patient-specific values for the characteristic cavity pressures  $EDP$  and  $ESP$ , respectively, as well as the stiffness parameters  $A$  and  $B$  for LV and RV. The corresponding physiologically motivated initial values are listed in Tab. 3. The LVM scaling parameters are set as  $\lambda^{LVM} = 1$  and  $\nu^{LVM} = 2$ , respectively and the stopping criterion of the cost function residual is chosen as  $\gamma_\epsilon^{LVM} = 1 \times 10^{-2}$ . The final obtained stiffness parameter and characteristic pressure values are listed in Tab. 4. The converged iterative parameter optimisation scheme gave for the unloaded LV cavity volumes  $V_0 = 86.66, 83.32$  and  $81.94$  mL and for the unloaded RV cavity volumes  $V_0 = 53.92, 65.18$  and  $86.99$  mL for cases 1, 2 and 3, respectively. Figs. 4 - 6 show the fitted EDPVR curves illustrating the FEM solutions by red lines and the targeted "Klotz curve" by blue circles indicating

Table 3: Initial material parameter and cavities pressure values in kPa Zhou et al. [2020], Mielniczuk et al. [2007], Wang et al. [2013]

	Left ventricle			Right ventricle		
	A (kPa)	B	<i>EDP</i>	A (kPa)	B	<i>EDP</i>
Case 1	0.10	1.00	2.00	0.10	1.00	0.50
Case 2	0.10	1.00	3.00	0.10	1.00	1.50
Case 3	0.10	1.00	2.00	0.10	1.00	2.50

Table 4: Final estimated material parameters and cavities pressure values in kPa.

	Left ventricle				Right ventricle			
	A (kPa)	B	<i>ESP</i>	<i>EDP</i>	A (kPa)	B	<i>ESP</i>	<i>EDP</i>
Case 1	0.10	1.25	0.04	1.78	0.11	1.05	0.08	0.85
Case 2	0.09	1.20	0.04	2.55	0.12	1.21	0.04	1.06
Case 3	0.09	1.07	0.04	1.72	0.10	0.88	0.02	1.25

good agreement. The root square mean error (RMSE) are 0.225, 0.225 and 0.375 mmHg for cases 1, 2 and 3 respectively at the LV and 0.150, 0.150 and 0.075 mmHg also for cases 1, 2 and 3 respectively.

The average percentage difference between the simulated and targeted CMR LVEDVs was approximately 0.0007%, and 0.0020% for the RVEDVs. Similarly, the average percentage difference between the simulated and targeted Klotz  $V_0$  for the LV was approximately 0.00005% and 5.3314% for the RV. The observed higher percentage error in the RV initial volume confirm that we did not target RV initial volume in our calibration. For the segmented and CMR ESV, there is 0.92% average error difference at the LV and 3.00% at the RV, detailed result is on Table. 5.

Table 5: Percentage error of LV and RV volumetric targets and results from the calibration.

	Left ventricle			Right ventricle		
	$V_0$	LVEDV	LVESV	$V_0$	RVEDV	RVESV
Case 1	0.00005	0.00172	1.42	1.73	0.0003	3.92
Case 2	0.00006	0.00029	0.01	0.01	0.0020	1.86
Case 3	0.00002	0.00005	1.33	14.25	0.0036	3.22

## 5.2 Stress and strain distributions

The contour plots in Figs. 7 and 8 reveal high myofibre stress and strain concentrations at the base which is to be expect due to the geometrical support. The global residual fibre stress, separately averaged over LV and RV myocardium,

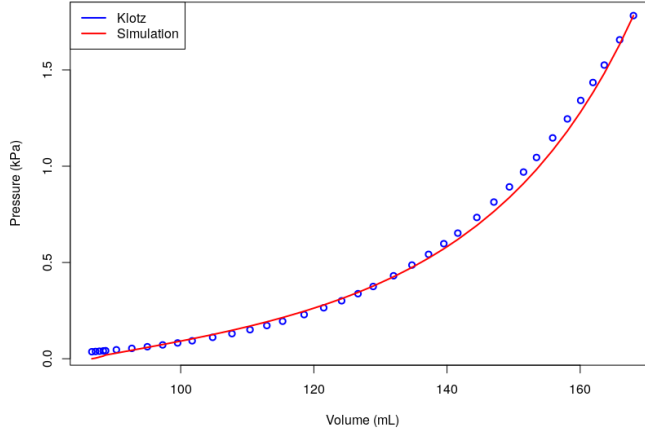


Figure 4: EDPVR curve predicted by Usyk model (red) and method of Klotz et al. (blue) as a physiological benchmark for case 1.

at end systole is found as 0.013, 0.018 and 0.006 kPa for LV at the longitudinal, circumferential and radial respectively and 0.031, 0.038, and 0.012 kPa for RV longitudinal, circumferential and radial respectively. A detailed analysis of regional strain in the LV with respect to the global longitudinal, circumferential and radial directions is presented. Endocardial strain comparison demonstrated moderate agreement of global strains, separately averaged over the LV and RV myocardium, respectively. Global longitudinal strain values (GLS) for cases 1 to 3 are 5.75, 6.90 and 7.14% for the FE model simulation, while the CMR in vivo recorded values for cases 1 to 3 are given as 12.30, 17.80 and 21.60% respectively. The global circumferential strain values (GCS) for the FE simulations are 22.2, 25.82 and 25.82%, and 20.20, 20.40 and 25.70% for the in vivo. Similarly, the global radial strain values (GRS) for the FE simulations are -15.84, -17.37, and -16.39%, and -13.90, -14.00, and -16.20% in vivo for the cases 1, 2 and 3 respectively. The GCS and GRS are well comparable in both FE model simulation and the CMR in vivo, but this was not the case with longitudinal strains, whereby a regional analysis of the longitudinal strains revealed poor agreement between simulated and measured in vivo strains. Although discrepancies have been noted between the FEM and in vivo longitudinal strain Sack et al. [2018] due to the absence of data on the true distribution of the patient-specific myofiber orientation angles, which affects the circumferential-longitudinal compliance ratio. Also the CMR long-axis scan providing longitudinal strain and the short-axis scan providing circumferential and radial strains are obtained from different cardiac cycles whereas the FEM calculate these strains using the same cardiac cycle.

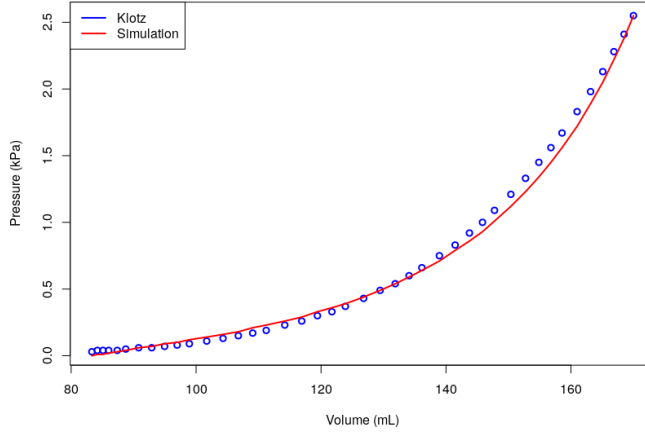


Figure 5: EDPVR curve predicted by Usyk model (red) and method of Klotz et al. (blue) as a physiological benchmark for case 2.

## 6 Conclusion

In this paper, a direct inverse method to determine the unloaded configurations of biventricular patient-specific heart models is combined with the bounded Levenberg-Marquart parameter optimisation method to estimate besides elastic material parameters also the unknown end-systolic and end-diastolic ventricular pressures *in silico*. The unloaded configuration is computed by a modified total Lagrangian approach as implemented in standard FEM which implicitly provides for the incorporation of pre-stressing and pre-straining of the myocardium as linked to the end-systolic pressure. The proposed variational principle is derived from the standard Lagrangian formulation, in contrast to the similar inverse unloaded configuration determination methods by Govindjee and Mihalic [1996] and Gee et al. [2010]. The unknown characteristic ventricular pressures and elastic material parameters can then be iteratively computed by taking advantage of the highly nonlinear exponential nature of the EDPVR and fitting the patient-specific LV EDPVR to the analytical volume-normalized "Klotz EDPVR curve". Making use of CMR-derived anatomical heart models, the iterative framework therefore provides the means to non-invasively estimate LV pressure, pre-strain and elastic material parameters exploiting their biomechanical interdependence.

Our results indicate good agreement between the EDPVR curves obtained from FE simulation and given by the "Klotz Curve". Additionally, there is a close agreement in the FE global circumferential and radial strains when compared with the CMR global strain data. The global longitudinal strain shows poor agreement between FE and CMR measured strains. This dis-



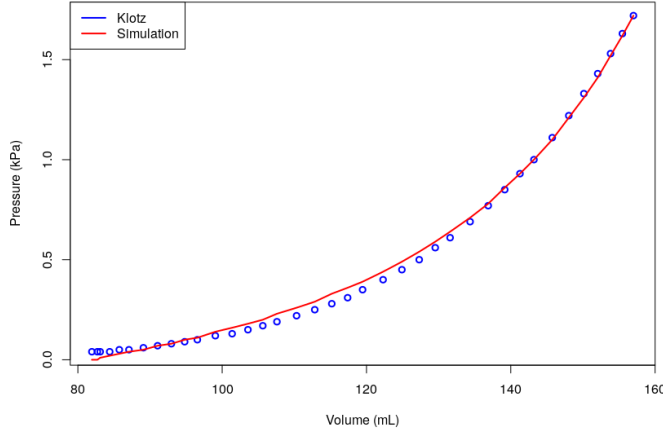


Figure 6: EDPVR curve predicted by Usyk model (red) and method of Klotz et al. (blue) as a physiological benchmark for case 3.

crepancy has been attributed to the absence of data on the true distribution of the patient-specific myofiber orientation distribution, which affects the circumferential-longitudinal compliance ratio Sack et al. [2018]. Also the CMR long-axis scan providing longitudinal strain and short-axis scan providing circumferential and radial strains are obtained from different cardiac cycles whereas FEM calculates these strains within the same cardiac cycle. Another limitation of this study is the absence of in vivo pressure measurements to validate our results. In future work, we shall obtain pressure data in vivo to perform validation of our proposed method, also patient-specific fiber orientation distribution data from DTMRI will help to mitigate the error in FE and CMR global longitudinal strains.

## References

- Brian Baillargeon, Nuno Rebelo, David D Fox, Robert L Taylor, and Ellen Kuhl. The living heart project: a robust and integrative simulator for human heart function. *European Journal of Mechanics-A/Solids*, 48:38–47, 2014.
- Joris Bols, Joris Degroote, Bram Trachet, Benedict Verheghe, Patrick Segers, and Jan Vierendeels. A computational method to assess the in vivo stresses and unloaded configuration of patient-specific blood vessels. *Journal of computational and Applied mathematics*, 246:10–17, 2013.
- Michael W Gee, Ch Förster, and WA Wall. A computational strategy for pre-stressing patient-specific biomechanical problems under finite deformation.

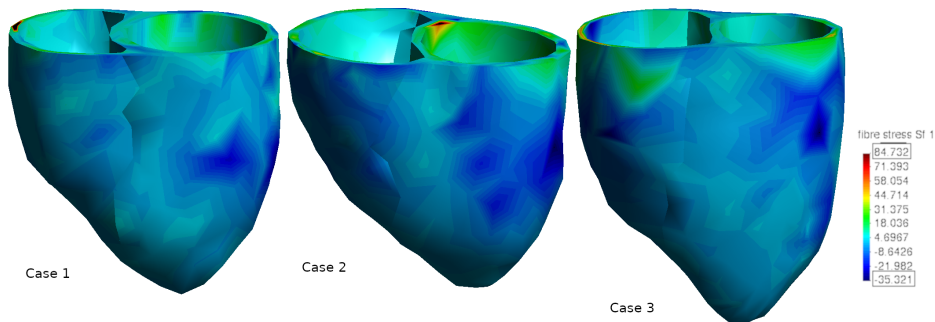


Figure 7: Fibre stress at the end-diastole.

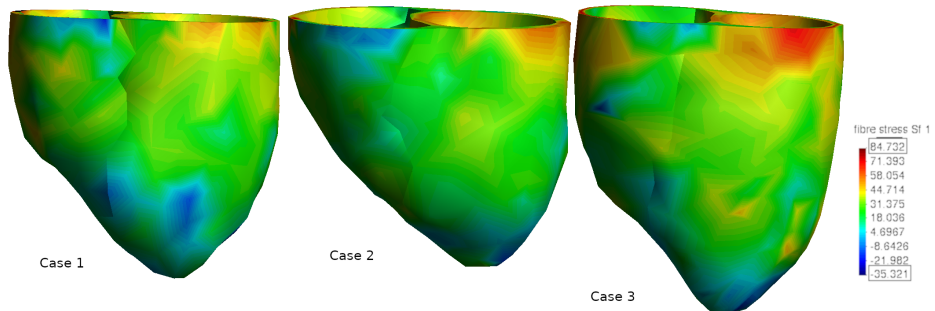


Figure 8: Fibre strain at the end-diastole.

*International Journal for Numerical Methods in Biomedical Engineering*, 26 (1):52–72, 2010.

Martin Genet, Lik Chuan Lee, Rebecca Nguyen, Henrik Haraldsson, Gabriel Acevedo-Bolton, Zhihong Zhang, Liang Ge, Karen Ordovas, Sebastian Kozzerke, and Julius M Guccione. Distribution of normal human left ventricular myofiber stress at end diastole and end systole: a target for in silico design of heart failure treatments. *Journal of applied physiology*, 117(2):142–152, 2014.

Sanjay Govindjee and Paul A Mihalic. Computational methods for inverse finite elastostatics. *Computer Methods in Applied Mechanics and Engineering*, 136 (1-2):47–57, 1996.

Richard A Gray and Pras Pathmanathan. Patient-specific cardiovascular computational modeling: diversity of personalization and challenges. *Journal of cardiovascular translational research*, 11:80–88, 2018.

Frédéric Guyon and Rodolphe Le Riche. Least squares parameter estimation and the levenberg-marquardt algorithm: Deterministic analysis, sensitivities and numerical experiments. Technical Report 041/99, Institut National des Sciences Appliquées, 2000.

- Marc Hirschvogel, Marina Bassilious, Lasse Jagschies, Stephen M Wildhirt, and Michael W Gee. A monolithic 3d-0d coupled closed-loop model of the heart and the vascular system: experiment-based parameter estimation for patient-specific cardiac mechanics. *International journal for numerical methods in biomedical engineering*, 33(8):e2842, 2017.
- Stefan Klotz, Ilan Hay, Marc L Dickstein, Geng-Hua Yi, Jie Wang, Mathew S Maurer, David A Kass, and Daniel Burkhoff. Single-beat estimation of end-diastolic pressure-volume relationship: a novel method with potential for non-invasive application. *American Journal of Physiology-Heart and Circulatory Physiology*, 291(1):H403–H412, 2006.
- Lisa M Mielniczuk, Gervasio A Lamas, Greg C Flaker, Gary Mitchell, Sidney C Smith, Bernard J Gersh, Scott D Solomon, Lemuel A Moyé, Jean L Rouleau, John D Rutherford, et al. Left ventricular end-diastolic pressure and risk of subsequent heart failure in patients following an acute myocardial infarction. *Congestive Heart Failure*, 13(4):209–214, 2007.
- Michael J Moulton, Lawrence L Creswell, Ricardo L Actis, Kent W Myers, Michael W Vannier, Barna A Szabo, and Michael K Pasque. An inverse approach to determining myocardial material properties. *Journal of biomechanics*, 28(8):935–948, 1995.
- Amir Nikou, Shauna M Dorsey, Jeremy R McGarvey, Joseph H Gorman, Jason A Burdick, James J Pilla, Robert C Gorman, and Jonathan F Wenk. Computational modeling of healthy myocardium in diastole. *Annals of biomedical engineering*, 44:980–992, 2016.
- JH Omens, AD McCulloch, and JC Criscione. Complex distributions of residual stress and strain in the mouse left ventricle: experimental and theoretical models. *Biomechanics and modeling in mechanobiology*, 1(4):267–277, 2003.
- Arnab Palit, Sunil K Bhudia, Theodoros N Arvanitis, Glen A Turley, and Mark A Williams. In vivo estimation of passive biomechanical properties of human myocardium. *Medical & biological engineering & computing*, 56:1615–1631, 2018.
- Mathias Peirlinck, Matthieu De Beule, Patrick Segers, and Nuno Rebelo. A modular inverse elastostatics approach to resolve the pressure-induced stress state for in vivo imaging based cardiovascular modeling. *Journal of the mechanical behavior of biomedical materials*, 85:124–133, 2018.
- Reza Pourmodheji, Zhenxiang Jiang, Christopher Tossas-Betancourt, C Alberto Figueroa, Seungik Baek, and Lik-Chuan Lee. Inverse modeling framework for characterizing patient-specific microstructural changes in the pulmonary arteries. *Journal of the mechanical behavior of biomedical materials*, 119:104448, 2021.

- Vijayaraghavan Rajagopal, Jae-Hoon Chung, David Bullivant, Poul MF Nielsen, and Martyn P Nash. Determining the finite elasticity reference state from a loaded configuration. *International Journal for Numerical Methods in Engineering*, 72(12):1434–1451, 2007.
- Ritesh R Rama, Sebastian Skatulla, and Carlo Sansour. Real-time modelling of diastolic filling of the heart using the proper orthogonal decomposition with interpolation. *International Journal of Solids and Structures*, 96:409–422, 2016.
- Ritesh Rao Rama and Sebastian Skatulla. Real-time nonlinear solid mechanics computations for fast inverse material parameter optimization in cardiac mechanics. *Journal of Engineering Mechanics*, 145(4):04019020, 2019.
- Kevin L Sack, Eric Aliotta, Daniel B Ennis, Jenny S Choy, Ghassan S Kassab, Julius M Guccione, and Thomas Franz. Construction and validation of subject-specific biventricular finite-element models of healthy and failing swine hearts from high-resolution dt-mri. *Frontiers in Physiology*, 9:539, 2018.
- Xiaodan Shi, Yue Liu, Katherine M Copeland, Sara R McMahan, Song Zhang, J Ryan Butler, Yi Hong, Michael Cho, Pietro Bajona, Huajian Gao, et al. Epicardial prestrained confinement and residual stresses: a newly observed heart ventricle confinement interface. *Journal of the Royal Society Interface*, 16(152):20190028, 2019.
- S Skatulla and C Sansour. On a path-following method for non-linear solid mechanics with applications to structural and cardiac mechanics subject to arbitrary loading scenarios. *International Journal of Solids and Structures*, 96:181–191, 2016.
- TP Usyk, R Mazhari, and AD McCulloch. Effect of laminar orthotropic myofiber architecture on regional stress and strain in the canine left ventricle. *Journal of elasticity and the physical science of solids*, 61(1):143–164, 2000.
- HM Wang, H Gao, XY Luo, C Berry, BE Griffith, RW Ogden, and TJ Wang. Structure-based finite strain modelling of the human left ventricle in diastole. *International journal for numerical methods in biomedical engineering*, 29(1):83–103, 2013.
- Jonathan F Wenk, Parastou Eslami, Zhihong Zhang, Chun Xu, Ellen Kuhl, Joseph H Gorman III, J Daniel Robb, Mark B Ratcliffe, Robert C Gorman, and Julius M Guccione. A novel method for quantifying the in-vivo mechanical effect of material injected into a myocardial infarction. *The Annals of thoracic surgery*, 92(3):935–941, 2011.
- Xia Zhou, Mingming Lei, Donghui Zhou, Guoqing Li, Zhiying Duan, Shaobo Zhou, and Yuanzhe Jin. Clinical factors affecting left ventricular end-diastolic pressure in patients with acute st-segment elevation myocardial infarction. *Ann Palliat Med*, 9(4):1834–1840, 2020.

X Zhuan and XY Luo. Volumetric growth of soft tissues evaluated in the current configuration. *Biomechanics and Modeling in Mechanobiology*, 21(2):569–588, 2022.